Journal of Materials Chemistry A

Accepted Manuscript

ROYAL SOCIETY OF CHEMISTRY

www.rsc.org/materialsA

Journal of Materials Chemistry A

PAPER

Hierarchical Porous Carbon Microtubes Derived from Willow Catkins for Supercapacitor Application

Received 00th January 20xx,
Accepted 00th January 20xx

DOI: 10.1039/x0xx00000x

www.rsc.org/

Lijing Xie[a], Guohua Sun[a], Fangyuan Su[a], Xiaoqian Guo[a], Qingqiang Kong[a], Xiaoming Li[a], Xianhong Huang[a], Liu Wan[a], Wen song[b], Kaixi Li[a], Chunxiang Lv[a], Cheng-Meng Chen[a]*

With willow catkins as highly accessible carbon sources, hierarchical porous carbon microtubes (denoted as HPNCTs) have been successfully prepared by a facile carbonization and subsequent KOH activation process. The resulting materials not only inherited the natural tubular morphology of the willow catkins, but also developed the hierarchical porous structure by activation, with nitrogen from the biomass been self-doped to the resulting carbon. A maximum specific surface area of 1775.7 $m^2 g^{-1}$ with pore volume of 0.8516 $cm^3 g^{-1}$ was achieved for HPNCT-800. As evaluated in a three electrode 6 M KOH system, the material exhibits a high gravimetric capacitance of 292 F g^{-1} at current density of 1 A g^{-1}, with good rate capability of 83.5% retention at 10 Ag^{-1}. HPNCT-800 was further employed in a coin-type symmetric device with 1 M $LiPF_6$ electrolyte, and exhibit high energy density of 37.9 W h kg^{-1} at power density of 700 W kg^{-1}, with excellent cycling stability with 90.6% retention after 4000 cycles. By taking advantage of the unique structure of abundant biomass from nature, this work shed a light for the creation of advanced porous carbon materials towards energy storage applications.

1. Introduction

The demand for supercapacitors with high power density, fast charge/discharge rate and long lifetime has substantially increased due to their promising applications in portable electronics, hybrid electric vehicles, and stand-by power systems.[1, 2] Based on the charge-storage mechanism, supercapacitors can be divided into two categories: one is the electrical double-layer capacitors (EDLC), of which the capacitance arises from the charge separation at an electrode/electrolyte interface; the other is the pseudocapacitors associated with faradaic reactions of the electro-active species on the surface of the electrode.[3] In most cases, these two mechanisms always work together. Activated carbons (ACs) are considered promising candidates for EDLCs because of their moderate cost, excellent chemical stability, and high electronic conductivity.[2] Recently, some other carbon materials, such as templated carbons,[4] carbon nanofibers,[5] carbon nanotubes,[6] and graphene,[7, 8] have also been employed as the supercapacitor electrodes due to their high surface area, porosity, electronic conductivity and chemical stability with low cost. Since electrostatic storage of electrical energy in EDLCs was achieved by accumulation of charges at the electrode/electrolyte interfaces, a suitable pore structure and a relatively large surface area are required for the storage of energy in EDLCs. Besides, it is well-known that the presence of surface functional and electrical conductivity that mainly depends on the carbonization process is closely related to the electrochemical performance.[9, 10]

Given the above consideration, hierarchically porous carbons (HPCs), with well-defined microstructure, good electric conductivity, tunable surface chemistry and interconnected micro-, meso- and macro- porous structure, become the promising electrode materials for supercapacitors.[11, 12] Furthermore, as the electron donor, moderate nitrogen doping on the carbon matrix is beneficial for improving the capacitance by faradaic reaction and optimized wettability.[13, 14] At present, various precursors, such as polyacrylonitrile,[15] polyaniline,[16] and polybenzoxazine,[17] have been applied to the preparation of nitrogen-doped porous carbons. But harmful and expensive precursors, or complex equipment involved in these syntheses drastically hamper their large-scale production for industry applications. Thus, the development of a

[a] Key Laboratory of Carbon Materials, Institute of Coal Chemistry, Chinese Academy of Sciences, Taiyuan 030001, PR China
[b] ShanXi XinHua Chemical Co., Ltd, Taiyuan 030008, PR China
[c]

simple and low-cost method to prepare nitrogen-enriched HPC is urgently required.

Towards this end, biomass becomes an attractive precursor, as the structure of which has been optimized by natural selection for millions of years. The transport channels of water and nutrients can be regarded as the template of porous structure carbon material. Meanwhile, the basic elements of biomass are carbon, sulfur, nitrogen and phosphorus. It is thus reasonable to expect that the controlled pyrolysis of biomass might obtain self-doped carbon materials. So the biomass-based carbon is expected to offer more fascinating performances compared with the artificially synthesized ones. Moreover, the biomass-based carbon is generally cheap, environmental friendly as well as readily available in high quality and quantity. For example, coconut shell is widely used in the production of commercial activated carbons.[18, 13] Moreover, more natural biomass materials, such as human hair,[19] leaves,[20] potassium citrate,[21] and Pistachio nutshell,[22] *etc.*, have been widely used to prepare hierarchical porous carbon, which not only greatly reduced the cost, but also inherited both of the structural flexibility and chemical diversity of the natural resources.

Willow, a genus of deciduous flowering trees, is widely planted in northern china. Interestingly, willow has the ability to absorb large amounts of nutrients to produce large quantities of catkins every spring. The catkins are white, lightweight, and flying around everywhere, as shown in Fig. 1. However, the flying willow catkins threaten to people's health in many ways, such as promoting runny nose, sneezing, shortness of breath, skin irritation to those with certain allergies, and it might even cause difficulty falling asleep. Therefore, it urgently needs to develop an environmentally friendly and economically feasible technology for utilizing the large scale of willow catkins. As shown in the insert of Fig. 2a and b, the willow catkins are in the micro-tubular structure, which can be served as the template of the carbon microtubes. On the other hand, fibrin and amino acid are the major constituents of willow catkins. The fibrin can be used as the carbon source for production of carbon materials, while the amino acids containing nitrogen atoms within their molecular structures, can be considered as nitrogen species to obtain self-doped carbon materials. Based on the above characteristics, willow catkin becomes highly appreciated carbon source. However, little attention has been paid to its role in practical applications for energy storage systems.

In this study, hierarchical porous nitrogen self-doped carbon microtubes are obtained by carbonization of the willow catkins in an inert gas and the subsequent KOH activation. The unique advantages of the synthetic strategy include the following: (i) naturally sustainable biomass that contains a large amount of organic and inorganic nitrogen is used as precursors; (ii) the synthetic procedure is simple and easy to handle without the need of additional templates and post-doping process, and (iii) the obtained carbon microtubes possess a large specific surface area, hierarchical porous distribution, and uniform nitrogen doping. Simultaneously, the electrochemical results demonstrate that the hierarchical porous carbon microtubes activated at 800 ^{o}C exhibits excellent capacitive property when adopted as the supercapacitor electrode. Such a low-cost as well as high-performance supercapacitor electrode material is potentially useful for high-power supercapacitors. Importantly, this would not only open a new way to convert the waste biomass into a high-value-added product, but also significantly decrease the emitted amounts of NO_x and CO_2 amounts.

2. Experimental Section

2.1. Synthesis of electrode materials

The preparation of hierarchical porous nitrogen-doped carbon microtubes was based on the carbonization of willow catkin followed by KOH activation. Detailed procedures are as follows: 6 g of the collected willow catkin was firstly washed with deionized water for several times, and then was marinated in 1 M HNO_3 for 12 h. Subsequently, the resulting material was washed thoroughly with deionized water and dried at 105 °C overnight in a vacuum oven. The dried willow catkin was further carbonized under a nitrogen atmosphere by heating at 600 °C for 4 h with a ramp rate of 1 °C min^{-1}. Then, the obtained carbonized material, named HPNCT, was thoroughly mixed in an aqueous KOH solution in a weight ratio of KOH:carbonized sample = 4:1, followed by water evaporation at 105 °C. The activation process was carried out at 600, 700, or 800 °C for 1 h in a tube furnace under flowing nitrogen with a ramp rate of 3 °C min^{-1}. The products were repeatedly washed with 1 M HCl and deionized water until the pH value of the filtrate reached about 7 and dried at 110 °C for 12 h. The obtained samples were named HPNCT-x, where x represents the activation temperature. For comparison, the sample named MPNC-800 was prepared by the simple one-step KOH activation of willow catkin at 800 °C.

2.2. Characterization

Scanning electron microscopy (SEM) investigations were carried out with a JEOL JSM-700 microscope instrument at an accelerating voltage of 10.0 kV. N_2 adsorption isotherms were measured. Before measurements were taken, all samples were degassed at 473 K for 12 h. The specific surface area was calculated by the Brunauer - Emmett-Teller (BET) method. The density functional theory (DFT) model assuming cylindrical-shaped pores was utilized to obtain the pore-size distribution (PSD). The PSD was also calculated based on the Barrett-Joyner-Halenda (BJH) model for mesopores. The thermogravimetric (TG) and derivative thermogravimetric (DTG) analyses were carried out on a Perkin-Elmer TG/DTG-6300 instrument in a temperature range of 30-900 °C. A heating rate of 10 C min^{-1} in air with a flow rate of 20 ml min^{-1} was used. The powder X-ray diffraction patterns were measured using a X-ray diffractometer (Bruker D8) with Cu Kα radiation (λ = 0.15406 nm). The Raman spectrums were obtained at ambient temperature on a Nanofinder 3.0 Raman spectrometer (Tokyo Instrument) using a visible laser beam of 488 nm as the excitation source. The elemental analysis was conducted with a Vario ELcube elemental analyzer. X-ray photoelectron spectroscopy (XPS) spectra were obtained on an AXIS Ultra DLD spectrometer with an excitation source of Mg Kα (1486.6 eV).

2.3. Electrochemical testing of HPNCTs in 6 M KOH

The test was firstly performed by using a three-electrode system in 6 M KOH aqueous electrolyte solution. A platinum foil and Hg/HgO electrode were used as the counter electrode and reference electrode, respectively. The working electrodes were prepared by mechanically mixing 80 wt% powered hierarchical porous nitrogen self-doped carbon microtubes, 10 wt% acetylene black, and 10 wt% polytetrafluoroethylene (PTFE) binder. Then the mixture was pressed on a 1 cm^{-2} nickel foam current collector and dried at room temperature for 24 h. The loading mass of HPNCTs on the electrode was 3.0 mg for each electrode. All electrochemical characterizations were carried out on a CHI760D electrochemical workstation. For quantitative considerations, the specific capacitance was calculated from the galvanostatic charge-discharge (GCD) values by using eq 1:

$$C=I\Delta t/\Delta mV \quad (1)$$

where C (F g^{-1}) is the specific capacitance, I (A) is the constant discharging current, ΔV (V) is the potential change within the discharge time Δt (s), and m (g) is the mass of the active material in the electrode.[23]

2.4. Electrochemical testing of the symmetric supercapacitors based on HPNCT-800 in 1 M $LiPF_6$

To construct the symmetrical supercapacitor based on HPNCT-800, electrodes were prepared by mixing 80 wt % amount of obtained HPNCT-800, 10 wt% acetylene black, and 10 wt% PVDF binder in N-methyl pyrrolidone to form slurry. The slurry was pasted on aluminum foil and then dried under vacuum at 120 ^oC for 6 h. After drying, the electrodes were cut into disks of 0.625 cm^2 in area. A 2 mg amount was loaded on an area of 0.625 cm^2. The two symmetrical electrodes were separated using a polypropylene separator soaked with 1 M $LiPF_6$ electrolytes in a CR2032 stainless steel coin cell. The cyclic voltammetry and galvanostatic charge-discharge tests for these devices were performed in the potential range of 0-2.8 V. Electrochemical impedance spectroscopy (EIS) was also performed in the frequency range of 10 kHz to 10 mHz at the open circuit voltage with an alternate current amplitude of 5 mV. The gravimetric capacitance for the single electrode was calculated according to eq 2:

$$C=4I\Delta t/\Delta mV \quad (2)$$

Where I (A) is the constant discharging current, ΔV (V) is the potential change within the discharge time Δt (s), and m (g) is the total mass of the active materials in the two electrodes. The energy density and power density of symmetrical supercapacitor systems were calculated by using eq 3 and 4:

$$E_t=1/2\ C_t(\Delta V)^2 \quad (3)$$

$$P_t=E_t/t \quad (4)$$

where E_t (W h kg^{-1}) is the specific energy density, P_t (W kg^{-1}) is the specific power density of the symmetrical supercapacitor system, C_t (F g^{-1}) I is the specific capacitance of the total symmetrical system, ΔV (V) is the cell voltage for charging and discharging, and t (h) is the discharge time, respectively.[24]

3. Results and discussion

3.1. Material characterization

Fig. 2 depicts the SEM images of willow catkin, pre-carbonized and subsequently KOH-activated samples. The catkin fibers show a hollow microtubular structure with a diameter of ~10 μm and a thickness of ~1 μm (Fig. 2a). Moreover, willow catkin microtubes have a smooth and clean surface with no apparently observed holes or cavities (Fig. 2b). After calcination and activation, these microtubes became brittle and tend to break to short pipes,

as shown in Fig. 2c-j. Notably, there is no obvious change in the morphology after the carbonization of catkin fibers (Fig. 2c and d), which still shows a smooth surface. Although HPNCT may exhibit some pores because of the pyrolysis of willow catkins and the evaporation of H_2O, CO_2 and NO_x during the carbonization process, the pores are not obvious in the typical SEM images. After the activation, SEM images of HPNCT-x indicate that a hollow microtubular structure (Fig. 2e-j) still maintains, but the surface morphologies of HPNCT600-HPNCT800, (Fig. 2i and j) were totally destructed by the etching of KOH. Interestingly, with the activation temperature increased from 600 to 800 °C, more mesoporous, microporous channels and macroporous cores developed in the walls of HPNCT800 and even interconnected with each other (Fig. 2j), which are helpful for the diffusion of an electrolyte ion into the inner micropores. These carbon microtubes were further characterized by transmission electron microscopy (TEM) (Fig.S2a and b), and meso/micropores and channels can be clearly seen. However, as shown in Fig. S1 (Support Information), MPNC-800 obtained by direct KOH activation of willow catkin exhibits the irregular granular aggregates, which is entirely different from the natural tubular morphology of willow catkins. Moreover, Fig.S3 compares the density of loose powders of HPNCT-800 with that of activated carbon derived coal and with that of graphene. The bulk density (tapped) of HPNCT-800 is about 0.36 g mL^{-1}, which is substantially lower than that of activated carbon derived coal (0.52 g mL^{-1}), being far larger than that of graphene (0.004 g mL^{-1}).

Further information on the specific surface area and pore structure of willow catkins, MPNC-800, HPNCT and HPNCT-xs (Fig. 3a and b) is obtained from N_2 adsorption-desorption isotherm measurements. It is clear that willow catkins show a type II sorption isotherm indicating the non-porous characteristic, while the isotherm profiles of MPNC-800 obtained by direct KOH activation of willow catkin at 800 °C completely overlap in the adsorption and desorption of N_2, exhibiting typical Type I isotherms, indicative of microporous structures.[6, 25] Compared with MPNC-800, the HPNCT-xs obtained by carbonization of willow catkin followed by KOH activation display I/IV-type adsorption desorption isothermal curves. A sharp rise of the N_2 isotherm can be observed at low relative pressures ($p/p_0<0.01$), indicating the existence of a large number of micropores. Meanwhile, A hysteresis loop extending from $P/P_0=0.5$ to 0.85 was also observed for the HPNCT-xs, suggesting the existence of mesopores in the samples. Furthermore, the obvious tails at high relative pressure ($p/p_0> 0.9$) denoted the formation of macropores within the carbons[26-28]. In a word, HPNCT-600, HPNCT-700, and HPNCT-800 exhibit hierarchical porous structures: abundant micropores, limited mesopores, and a few macropores. This may be due to a well-developed narrow microporosity of the pre-carbonized HPNCT sample as shown in Fig. 3a. These nanopores created by pre-carbonization process could provide abundant channels to accommodate KOH, making the dispersion of activation agents within the porosities of HPNCT more homogeneously and the following activation step more effectively. Furthermore, the inorganic components, for example, the silicate and metals ions,[29] of the biomass can be dissolved by the molten salts, resulting in more meso pores. The porous properties of these materials are summarized in Table 1, including the specific surface area (BET), total pore volume, and average pore diameter. With the activation temperatures increasing, the BET surface area and the pore volume both increase dramatically due to the deepened activation degree, from 350.61 m^2 g^{-1} and 0.2381cm^3 g^{-1} for HPNCT to 1775.7 m^2 g^{-1} and 0.8516 cm^3 g^{-1} for HPNCT-800, respectively. The average pore diameter decreased slightly from 2.58 to 1.9 nm with an increase of the activation temperature from 600 to 800 °C, indicating that larger micropores appeared by KOH etching under severe activation conditions. The trend could be further demonstrated by the pore size distribution obtained by the BJH method (Fig. 3b). Furthermore, mesopores and macropores with size ranging from 16 to 60 nm for HPNCT-600, HPNCT-700, and HPNCT-800 were created by KOH corrosion and volatilization of unstable nitrogen and oxygen functionalities at high temperature. By the same KOH-activation conditions, the pore size distribution of MPNC-800 is centered at 1.5 nm with a range of around 0.57-4 nm. These results reveal that pre-carbonization process treatment is critical to obtain HPNCT-800 with hierarchical structure and high specific surface area. Besides, the electrical conductivity of the HPNCT-800 based electrode is 35.84 S m^{-1}, which is superior than previously reports related to other biomass-based porous carbon.[20, 21] Other criterions that should be considered are the carbon yield and ash of the waste biomasses. The carbon yields of HPNCT-x are all around 20%, but that of MPNC-800 is only 17.5%, indicating molten salts remarkably affect the pyrolysis at higher temperatures, decreasing the apparent carbon yield. The ash content of HPNCT-800 determined from thermogravimetric (TG) was about 1.5%, as shown in

Fig.S4. Based on the above analysis, it is confirmed that the as-prepared HPNCT-800 should have a high specific capacitance and rate capability when used as the electrode material in supercapacitors.

The X-ray diffraction (XRD) pattern of the HPNCT and HPNCT-x can be seen in Fig. 4a. Two broad peaks at approximately 22.3° and 43.8° can be attributed to the (002) and (100) reflections of the disordered carbon layer. The high intensity in the low angle region indicates the existence of abundant micropores in the samples, which is consistent with the results of the N_2 adsorption-desorption measurements.[30] Furthermore, with the activation temperature increasing from 600 to 800 °C, the intensity of the (100) peak is gradually enhanced, implying the improvement of the graphitization degree of HPNCT-800. The Raman spectrums of the HPNCT and HPNCT-x are displayed in Fig. 4b. Two strong peaks at 1345 cm^{-1} (D band) and 1592 cm^{-1} (G band) are observed for all carbon materials. The D band refers to the disordered and imperfect structures in the carbonaceous materials, and the G band is related to the vibration of a sp^2-hybridized carbon in the graphite crystallites. The ratio of the relative intensity of the D band and G band (ID/IG) represents the graphitic degree of the carbon materials.[31, 32] From the spectrums in Fig. 4, the ID/IG ratio of HPNCT, HPNCT-600, HPNCT-700, and HPNCT-800 was estimated to be 1.08, 1.04, 0.98, and 0.91, respectively. The relatively lower D/G intensity ratio for HPNCT-800 indicates the higher degree of graphitization and a decrease of the disordered structure. This can be attributed to the loss of nitrogen and oxygen species at high activation temperature. These results are in good agreement with XRD analysis.

The chemical composition of the as-prepared carbon materials was determined by elemental analysis (EA), as shown in Table 2. It can be seen that all samples contain relatively high oxygen species (7.81-12.43 wt%) and nitrogen species (1.56-2.26 wt %). The contents of the nitrogen and oxygen atoms in HPNCT-xs decreased evidently with an increase of the activation temperature because of the poor thermal stability of the nitrogen and oxygen species at high temperature. The nature of the nitrogen and oxygen species on the surface of the carbon materials was further studied by XPS analysis (Fig. 5). The XPS survey spectra in Fig. 5a confirm the coexistence of C, N and O. Fitting the spectra to each element suggests that the obtained samples contain primarily carbon (82.42-91.51 at%) with small amounts of nitrogen (0.88-1.41 at%) and oxygen (7.08-16.4 at%), which are comparable with the EA results. The high-resolution N 1s spectrum (Fig. 5b) can be resolved into four individual peaks centered at 398.2-398.5 eV, 400.1-400.2 eV, 401 eV and 403.2-403.5 eV, referring to pyridinic-N, pyrrolic/pyridone-N, quaternary-N and pyridine-N-oxide,[33-35] as shown in Fig. 5b and Table 2. Data provided in this table reveals that the pyridinic-N and pyrrolic/pyridone-N are predominant (more than 60% of the total nitrogen atoms) for all samples. It is reported that the pyridinic-N and pyrrolic/pyridone-N are considered to be electrochemically active in an alkaline aqueous solution to provide main pseudocapacitance, which is significant for nitrogen-doped carbon materials to increase the capacitance.[36] Besides, the presence of quaternary-N, which are inset into the carbon matrix and bonded to three carbon atoms, can effectively benefit electron transfer and improve the conductivity of carbonaceous materials.[37] Thus, it can be inferred that HPNCT-800 with the highest quaternary-N content exhibits better conductivity than other samples. There are also two fitted peaks in the O 1s spectrum (Fig. 5c) positioned at 531.3-531.7 and 533.1-533.7, which may respectively represent C=O and C–O bands.[38] Therefore, these surface nitrogen- and oxygen-containing functional groups in the HPNCT-xs can not only generate great pseudocapacitance but also improve the wettability of the HPNCT-xs based electrodes in the aqueous electrolytes.

3.2. Electrochemical characterization

The electrochemical performance of the non-activated HPNCT and KOH-activated HPNCT-x as electrode materials for supercapacitors was measured in a three-electrode system with 6 M KOH as an aqueous electrolyte. As shown in Fig. 6a, the non-activated HPNCT presents triangle-like CV and its current density is much lower compared to other samples, indicating a small capacitance. Although HPNCT contains the largest number of nitrogen and oxygen species in the four samples, the low specific surface area and less developed porosity of HPNCT make it difficult for fast charge transfer during the Faradaic reactions and result in poor capacitive behavior. Much better CV curves could be found for the HPNCT-600 and HPNCT-700 samples. Quasi-rectangle shape curve was observed from the CV data for HPNCT-800, indicating the best electrochemical property of HPNCT-800 sample among the HPNCT and HPNCT-X samples. Noticeably, a slight hump around -0.8 V in all curves is observed, probably due to redox reactions of the doped heteroatoms such as nitrogen and oxygen functional groups. Moreover, we also investigated the rate-dependent CV curves for HPNCT-800 over a range of scan rates from 5 to 200 mV s^{-1} (Fig. 6b). The CV curve still retains a rectangular shape

and undergoes no change even at a high scan rate of 200 mV s^{-1}, indicating a quick charge propagation capability and facile ion transport within HPNCT-800 electrode materials. If the ions from the electrolyte are able to easily approach the electrochemically actives surface of the electrode, the charge-discharge capability become faster with the increase of the scan rate, which indicates the favorable reversibility of a supercapacitor.[39]

The capacitive performances for all four electrodes were further measured with galvanostatic experiments, as shown in Fig. 6c. It can be see that the discharge curve of the non-activated electrode exhibits the shortest discharge time among as-prepared samples and even non-linear charge-discharge curve at the same current density. In contrast, the charge-discharge curves of the KOH-activated electrodes are nearly linear and symmetrical with slight curvature, indicating a good capacitive behavior of electrical double layer capacitance (EDLC) and little pseudo-capacitance. Especially for the HPNCT-800 electrode, it also shows the longest discharge time. Given the excellent charge-discharge behaviors of the HPNCT-800 sample, we specially investigated its galvanostatic charge-discharge curves over a range of current densities from 1 to 10 A g^{-1} (Fig. 6d). All charge-discharge curves of the HPNCT-800 sample at various current densities are quasi-triangular and symmetrical, indicating an excellent capacitive behavior and electrochemical reversibility, which is consistent with the CV results. For comparison, Fig. 6e provides the capacitance retention of MPNC-800, HPNCT and HPNCT-xs at a range of current density from 1 to 10 Ag^{-1}. It is found that specific capacitance decrease when the current density is enhanced, which is related to the increase of diffusion limitation. As shown in Fig. 6e, HPNCT-800 exhibits excellent capacitance retention. Even at a high current density of 10 A g^{-1}, HPNCT-800 still maintained specific capacitances of 244 F g^{-1} with a capacitance retention ratio of 83.5%, which is much higher than that of other samples. The superior performances of HPNCT-800 are attributed to the following reasons. Firstly, the high specific area with abundant micropores is favorable for improving electrolyte contact and accumulating more electrolyte ions, and thus enhances the charge storage density. Secondly, the N-doping and oxygen-containing groups which improved the wettability and electrical conductivity and thus offer minimized diffusive resistance to electrolyte ion transport. Lastly, the presence of meso/macropores in HPNCT-800 not only makes the inner micropore surface more electrochemically accessible for electrolyte ions and more charges to be accumulated in the micropores but also facilitates the fast diffusion of electrolyte ions in the pore channels at high current densities.

In order to explore supercapacitors for its broad applications at high energy density, we constructed and measured the performance of two-electrode symmetrical supercapacitor cell on the basis of HPNCT-800 and 1 M $LiPF_6$ electrolyte, as shown in Fig. 7. The typical rectangular CV curve from 0 to 2.8 V was obtained even at a high scan rate of 200 mV s^{-1} (Fig. 7a), indicating fast and efficient charge transfer. The galvanostatic charge-discharge curves at different current density over the voltage window of 0-2.8 V were also measured to determine the specific capacitance, as presented in Fig. 7b. The linear and nearly symmetric charge-discharge curves without an obvious IR drop further reveal good capacitive characteristics for the as-fabricated supercapacitor. As can be seen in Fig. 7c, the specific capacitance (for a single electrode) of supercapacitor is calculated to be 139 F g^{-1} at a current density of 1 A g^{-1}, and this value is still as high as 88 F g^{-1} with a retention of 63.3% at a high current density of 10 A g^{-1}, which is much higher or at least comparable to most of the carbons derived from human hair,[19] leaves,[20] potassium citrate,[21] and Pistachio nutshell [22] (126 F g^{-1} at 1 A g^{-1}, and 88 F g^{-1} at 2 A g^{-1}, and 138 F g^{-1} at A g^{-1}, and 97 F g^{-1} at 8 A g^{-1}). Fig. 7d gives further evidence that the as-fabricated cell shows an almost vertical curve in the low frequency region, indicating a nearly ideal capacitive behavior. From the magnified data in the high-frequency range (Fig. 7d, insert), the intercept at the real axis at high frequencies is the equivalent series resistance value of about 1.44 V, showing good electric conductivity. A small semicircle is obtained at the high-frequency region. It is well accepted that a semicircle reflects the electrochemical reaction impedance of the electrode, and a smaller semicircle means smaller charge transfer resistance.40 Moreover, a transition between the small semicircle and the migration of electrolyte was observed at a frequency of about 2686 Hz, corresponding to a resistance of 3.46 ohms. The inclined portion of the curve (about 45^{o}) in the low frequency is ascribed to the Warburg impedance, which is related to ion diffusion/transport in the electrolyte. The diffusion of electrolyte ions stopped at about 122 Hz, and thereafter the whole capacitance was reached.[41]

The cycling stability of the HPNCT-800//HPNCT-800 symmetric electrochemical capacitor in 1 M $LiPF_6$ electrolyte was further investigated by the galvanostatic charge-discharge between 0 and 2.8 V at a current density of 1 A g^{-1} (Fig. 8a). After 4000 cycles, the specific

capacitance of the as-fabricated symmetric supercapacitor decreased from 139 to 126 F g^{-1}, with a capacitance retention ratio of 90.6%, displaying an excellent long-term cycling durability. The cycling durability of the symmetric supercapacitor can be confirmed by the galvanostatic charge-discharge curves of after cycle inserted in Fig. 8a, which maintain nearly symmetric the same as that of before cycle. Ragone plots relating the energy density to the power density are an efficient way to evaluate the capacitive performance of supercapacitor cells. The energy density and the power density for a supercapacitor cell can be calculated *via* eqs 3 and 4. The Ragone plot for the HPNCT-800//HPNCT-800 symmetric electrochemical capacitor in 1 M LiPF6 electrolyte is presented in Fig. 8b. The specific energy density for the device is about 37.9 W h kg^{-1} at a current density of 1 A g^{-1}. It is noteworthy to mention that specific energy density is still 24 W h kg^{-1} with a high power density of 7 kW kg^{-1} at a current density of 10 A g^{-1}, which is superior to the commercial devices (<3 W h kg^{-1}).[42] A comparison of specific energy and power density is shown in Table 4. It can be seen that the energy and power density of the carbon derived from willow catkins is superior or at least comparable to other waste biomass derived carbons.[19, 22, 26, 43] Furthermore, two as-fabricated CR2032 coin-type symmetric supercapacitors in series can drive an LED bulb brightly for 10 minutes after charging for only 10 seconds, which reveals its practical application in energy storage. In summary, we have demonstrated the successful use of willow catkins microtubes to construct hierarchical porous nitrogen self-doped carbon microtubes electrodes for supercapacitor with excellent capacitive performances, which will open a simple and environmentally sound way for changing willow catkin into value-added capacitive carbon to reduce its hazards to people's life in many ways (see Fig. 8b).

4. Conclusions

The hierarchical porous nitrogen-doped carbon microtubes (HPNCT) were prepared by a simple carbonization of willow catkin followed by KOH activation. The as-obtained HPNCT-800 processes an inherited the natural tubular structure with proper porosity, high specific surface area (1775.7 m^2 g^{-1}), a small amount of nitrogen-doping (1.56%) and excellent electrical conductivity (35.84 S m^{-1}). As the electrode material for supercapacitor, HPNCT-800 exhibits a high specific capacitance of 292 F g^{-1} at a current density of 1 A g^{-1} and a good rate capability with a retention of 83.5% at 10 Ag^{-1} in 6 M KOH. More importantly, a high energy density of 37.9 W h kg^{-1} at a current density of 1 A g^{-1}, and a stable cycle life over 4000 cycle for 2.8 V working voltage were achieved in a fully packaged symmetric supercapacitor based on the HPNCT-800 in the 1 M $LiPF_6$ electrolyte. These high performances demonstrate that the hierarchical porous carbon derived from willow catkins is a good potential material in energy conversion and storage devices. The synthesis strategy developed in this work could also open up a route to prepare advanced energy materials from renewable biomass waste.

Acknowledgements

We gratefully acknowledge the support of this work by National Nature Science Foundation of China (No. 51402324, 51402325, 51302281), Innovative Research Fund of ICC-CAS (2012SCXQT03), Natural Science Foundation of Shanxi Province (2015021077, 2013011012-7), Innovative Research Fund of Taiyuan Science and Technology Bureau (2012CXJD0510), Shanxi Coal Transportation and Sales Group Co. Ltd (2013WT103). Furthermore, we thank Ms. Zhuo Liu for a significant improvement in language with the whole manuscript.

Notes and references

1 R. Zhang, Q. Wen, W. Qian, D. S. Su, Q. Zhang and F. Wei, *Adv. Mater.*, 2011, **23**, 3387-+.
2 L. L. Zhang and X. S. Zhao, *Chem. Soc. Rev.*, 2009, **38**, 2520-2531.
3 P. Simon and Y. Gogotsi, *Nat. Mater.*, 2008, **7**, 845-854.
4 Y. Zhai, Y. Dou, D. Zhao, P. F. Fulvio, R. T. Mayes and S. Dai, *Adv. Mater.*, 2011, **23**, 4828-4850.
5 B. Xu, F. Wu, R. Chen, G. Cao, S. Chen and Y. Yang, *J. Power Sources*, 2010, **195**, 2118-2124.
6 Y. J. Kang, S.-J. Chun, S.-S. Lee, B.-Y. Kim, J. H. Kim, H. Chung, S.-Y. Lee and W. Kim, *ACS Nano*, 2012, **6**, 6400-6406.
7 Q.-Q. Kong, C.-M. Chen, Q. Zhang, X.-H. Zhang, M.-Z. Wang and R. Cai, *J. Phys. Chem. C*, 2013, **117**, 15496-15504.
8 C.-M. Chen, Q. Zhang, X.-C. Zhao, B. Zhang, Q.-Q. Kong, M.-G. Yang, Q.-H. Yang, M.-Z. Wang, Y.-G. Yang, R. Schloegl and D. S. Su, *J. Mater. Chem.*, 2012, **22**, 14076-14084.
9 F. Su, C. K. Poh, J. S. Chen, G. Xu, D. Wang, Q. Li, J. Lin and X. W. Lou, *Energy Environ. Sci.*, 2011, **4**, 717-724.
10 X. Zhao, Q. Zhang, C.-M. Chen, B. Zhang, S. Reiche, A. Wang, T. Zhang, R. Schloegl and D. S. Su, *Nano Energy*, 2012, **1**, 624-630.
11 T. C. Chou, R.A. Doong, C.C. Hu, B. Zhang and D. S. Su, *Chemsuschem*, 2014, **7**, 841-847.
12 D. W. Wang, F. Li, M. Liu, G. Q. Lu and H. M. Cheng, *Angew. Chem.-Int. Edit.*, 2009, **48**, 1525-1525.

13 D. Hulicova-Jurcakova, M. Seredych, G. Q. Lu and T. J. Bandosz, *Adv. Funct. Mater.*, 2009, **19**, 438-447.
14 H. M. Jeong, J. W. Lee, W. H. Shin, Y. J. Choi, H. J. Shin, J. K. Kang and J. W. Choi, *Nano Lett.*, 2011, **11**, 2472-2477.
15 C. Kim, B. T. N. Ngoc, K. S. Yang, M. Kojima, Y. A. Kim, Y. J. Kim, M. Endo and S. C. Yang, *Adv. Mater.,* 2007, **19**, 2341-+.
16 J. Yan, T. Wei, W. Qiao, Z. Fan, L. Zhang, T. Li and Q. Zhao, *Electrochem. Commun.*, 2010, **12**, 1279-1282.
17 N. N. Ghosh, B. Kiskan and Y. Yagci, *Prog. Polym. Sci.*, 2007, **32**, 1344-1391.
18 K. Jurewicz and K. Babel, *Energy & Fuels*, 2010, **24**, 3429-3435.
19 W. Qian, F. Sun, Y. Xu, L. Qiu, C. Liu, S. Wang and F. Yan, *Energy Environ. Sci.*, 2014, **7**, 379-386.
20 M. Biswal, A. Banerjee, M. Deo and S. Ogale, *Energy Environ. Sci.*, 2013, **6**, 1249-1259.
21 M. Sevilla and A. B. Fuertes, *ACS Nano*, 2014, **8**, 5069-5078.
22 J. Xu, Q. Gao, Y. Zhang, Y. Tan, W. Tian, L. Zhu and L. Jiang, *Sci. Rep.*, 2014, **4**.
23 G. Wang, J. Huang, S. Chen, Y. Gao and D. Cao, *J. Power Sources,* 2011, **196**, 5756-5760.
24 J. Zhang and X. S. Zhao, *Chemsuschem*, 2012, **5**, 818-841.
25 C. Z. Yuan, B. Gao, L. F. Shen, S. D. Yang, L. Hao, X. J. Lu, F. Zhang, L. J. Zhang and X. G. Zhang, *Nanoscale*, 2011, **3**, 529-545.
26 Q. H. Liang, L. Ye, Z. H. Huang, Q. Xu, Y. Bai, F. Y. Kang and Q. H. Yang, *Nanoscale*, 2014, **6**, 13831-13837.
27 Y. W. Ma, J. Zhao, L. R. Zhang, Y. Zhao, Q. L. Fan, X. A. Li, Z. Hu and W. Huang, *Carbon*, 2011, **49**, 5292-5297.
28 A. C. Lua, F. Y. Lau and J. Guo, *J. Anal. Appl. Pyrol.*, 2006, **76**, 96-102.
29 J. S. Le Blond, S. Strekopytov, C. Unsworth and B. J. Williamson, *Anal. Methods*, 2011, **3**, 1752-1758.
30 Y. Zhu, S. Murali, M. D. Stoller, K. J. Ganesh, W. Cai, P. J. Ferreira, A. Pirkle, R. M. Wallace, K. A. Cychosz, M. Thommes, D. Su, E. A. Stach and R. S. Ruoff, *Science*, 2011, **332**, 1537-1541.
31 K. Ai, Y. Liu, C. Ruan, L. Lu and G. Lu, *Adv. Mater.*, 2013, **25**, 998-1003.
32 Q. Wang, J. Yan, Y. Wang, G. Ning, Z. Fan, T. Wei, J. Cheng, M. Zhang and X. Jing, *Carbon*, 2013, **52**, 209-218.
33 B. Xu, S. S. Hou, G. P. Cao, F. Wu and Y. S. Yang, *J. Mater. Chem.*, 2012, **22**, 19088-19093.
34 M. Seredych, D. Hulicova-Jurcakova, G. Q. Lu and T. J. Bandosz, *Carbon*, 2008, **46**, 1475-1488.
35 Y. H. Lee, Y. F. Lee, K. H. Chang and C. C. Hu, *Electrochem. Commun.*, 2011, **13**, 50-53.
36 C. O. Ania, V. Khomenko, E. Raymundo-Pinero, J. B. Parra and F. Beguin, *Adv. Funct. Mater.*, 2007, **17**, 1828-1836.
37 J. Wu, D. Zhang, Y. Wang and B. Hou, *J. Power Sources*, 2013, **227**, 185-190.
38 L. Qie, W. Chen, H. Xu, X. Xiong, Y. Jiang, F. Zou, X. Hu, Y. Xin, Z. Zhang and Y. Huang, *Energy Environ. Sci.*, 2013, **6**, 2497-2504.
39 N. D. Kim, W. Kim, J. B. Joo, S. Oh, P. Kim, Y. Kim and J. Yi, *J. Power Sources,* 2008, **180**, 671-675.
40 L. Yang, S. Cheng, Y. Ding, X. Zhu, Z. L. Wang and M. Liu, *Nano Lett.*, 2012, **12**, 321-325.
41 P. L. Taberna, P. Simon and J. F. Fauvarque, *J. Electrochem. Soc.*, 2003, **150**, A292-A300.
42 Y. Gogotsi and P. Simon, *Science*, 2011, **334**, 917-918.
43 E. Raymundo-Pinero, M. Cadek and F. Beguin, *Adv. Funct. Mater.*, 2009, **19**, 1032-1039.

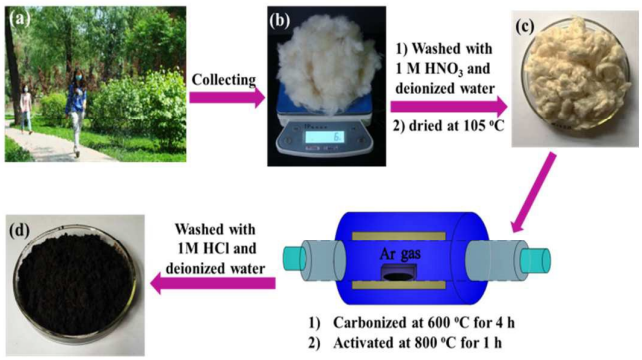

Fig. 1 Preparation of the hierarchical porous nitrogen self-doped carbon microtubes. Images of the flying willow catkins (a), the collected willow catkons (b), raw material for carbonized process (c), product HPNCT-800 (e).

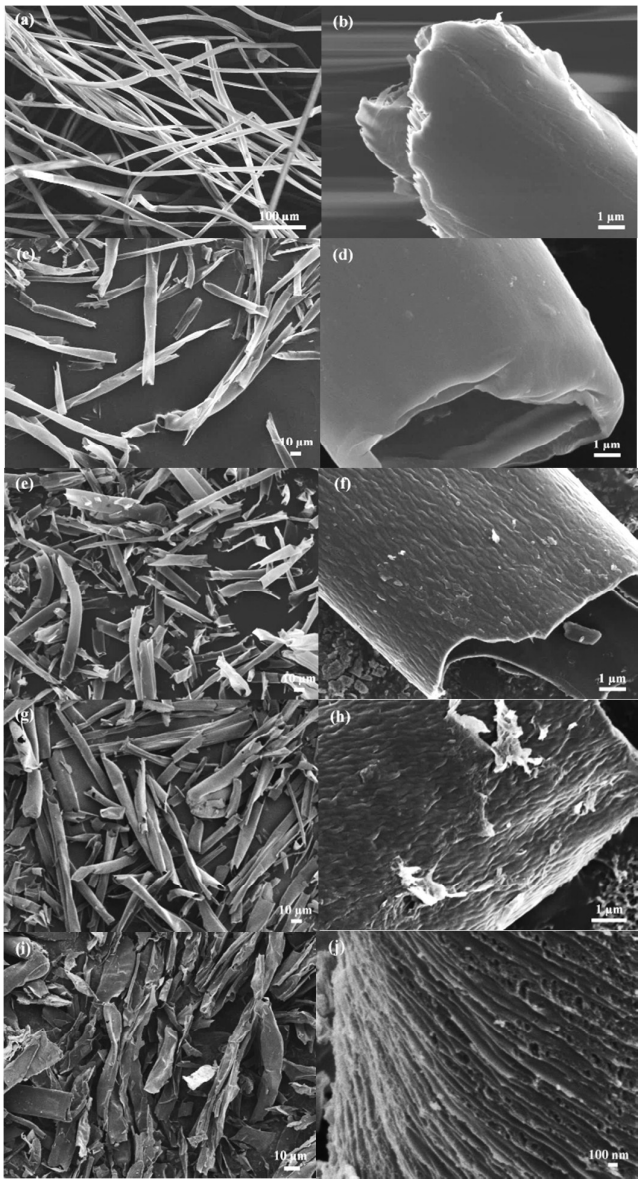

Fig.2. SEM images of (a, b) willow catkin, (c, d) pre-carbonized HPNCT, (e, f) HPNCT-600, (g, h) HPNCT-700, and (i, j) HPNCT-800.

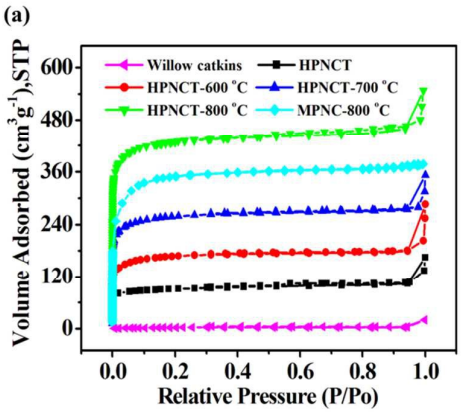

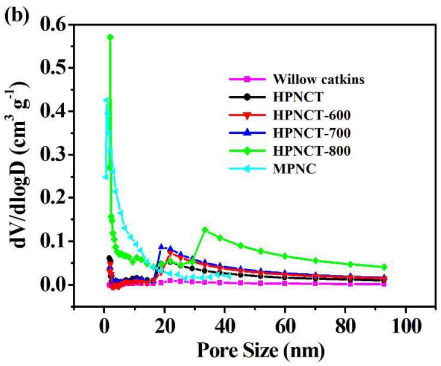

Fig.3. Nitrogen adsorption desorption isotherms (a) and pore size distribution (b) of willow catkins, MPNC-800, HPNCT, HPNCT-600, HPNCT-700, and HPNCT-800.

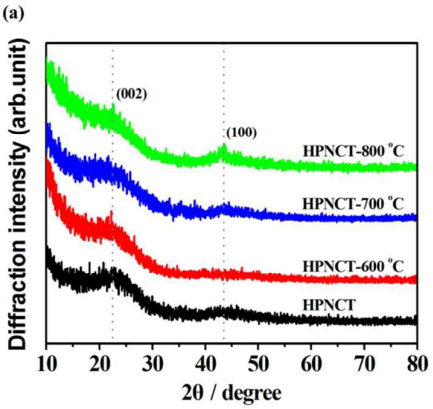

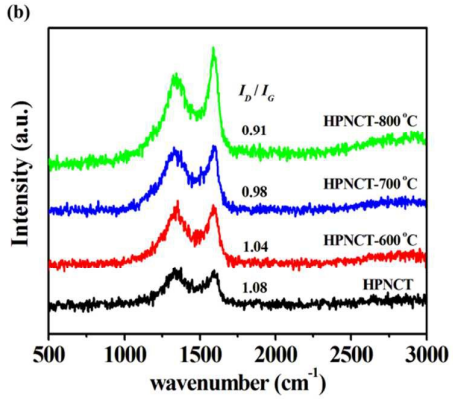

Fig.4. XRD patterns (a) and Raman spectra (b) of HPNCT, HPNCT-600, HPNCT-700, and HPNCT-800.

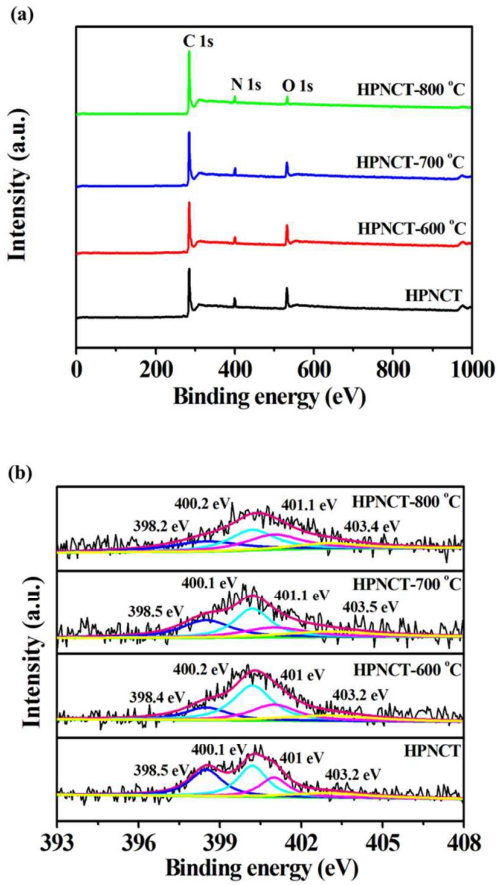

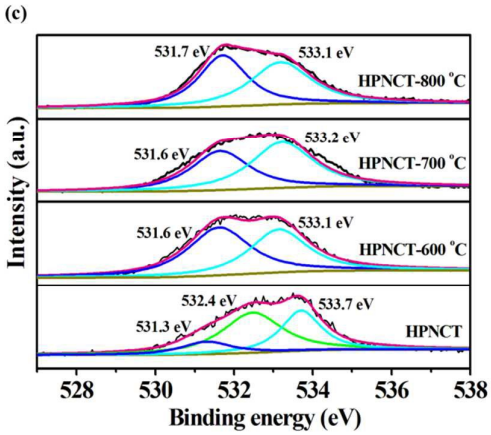

Fig.5. XPS spectra of HPNCT, HPNCT-600, HPNCT-700, and HPNCT-800: (a) survey spectra; (b) N 1s; (c) O 1s.

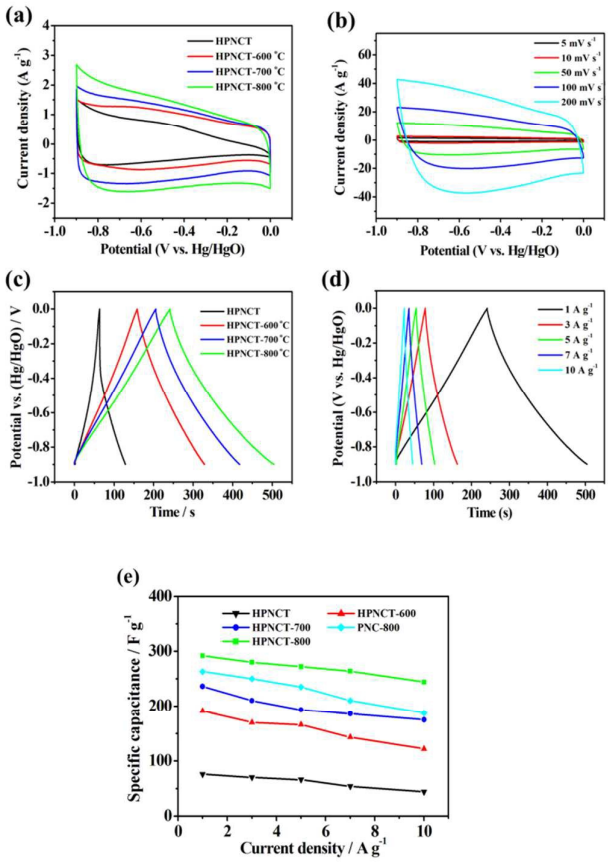

Fig.6. Electrochemical performance of the as-prepared carbon electrodes measured in a three-electrode system: (a) CV curves for HPNCT, HPNCT-600, HPNCT-700, and HPNCT-800 at scan rates of 5 V s^{-1} and (b) the rate-dependent CV curves for HPNCT-800 over a range of scan rates from 5 to 200 mV s^{-1}; (c) GCD curves for HPNCT, HPNCT-600, HPNCT-700, and HPNCT-800 at current densities of 1 A g^{-1} and (d) GCD curves for HPNCT-800 over a range of current densities from 1 to 10 A g^{-1}; (e) Specific capacitance as a function of the discharge current density for all samples.

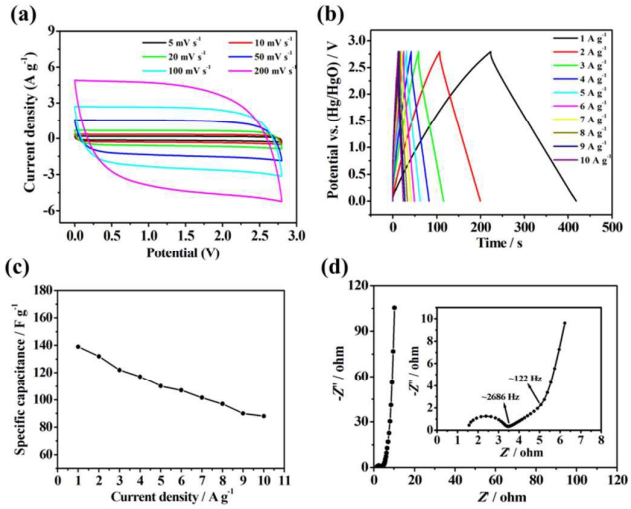

Fig.7. Electrochemical performance of HPNCT-800 in a two-electrode system using 1 M $LiPF_6$ electrolyte. (a) CV curves at various scan rates; (b) GCD curves at different current densities; (c) Specific capacitance as a function of the current densities; (d) Nyquist plots in the frequency range of 10 mHz to 100 kHz.

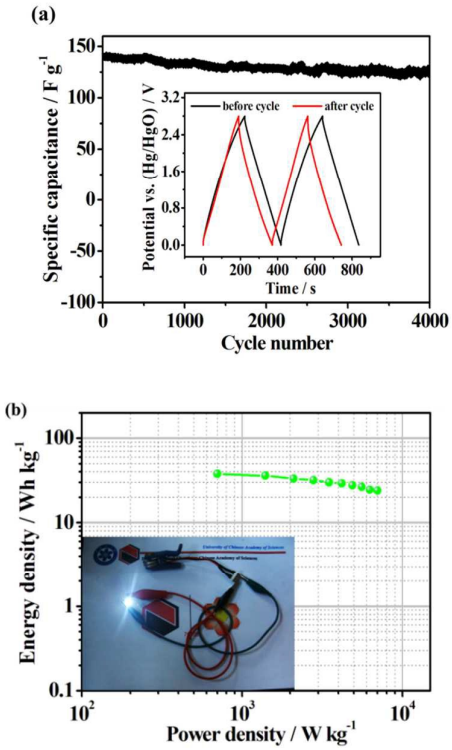

Fig.8. Cycling stability at a current density of 1 A g^{-1} up to 4000 cycles (a) and Ragone plot of symmetrical HPNCT-800 based supercapacitors (b). Insert shows a good example for changing willow catkin into value-added capacitive carbon: two as-fabricated CR2032 coin-type symmetric supercapacitors in series with willow catkin-based carbon as electrodes can light up a LED bulb brightly.

Table 1. Textual parameters of the Samples

Items	Willow catkins	HPNCT	HPNCT -600	HPNCT -700	HPNCT -800	MPNC-800
BET surface area (m2 g^{-1})	1.9	350.61	638.72	1012.2	1775.7	1540
Total pore volume (cm3g^{-1})	0.0549	0.2381	0.4124	0.5234	0.8516	0.5874
Average pore diameter (nm)	115.77	2.72	2.58	2.07	1.92	1.52
Yield (wt.%)	----	29.8	24.8	21.4	20.8	17.5

Table 2. Elemental and XPS Analysis of the Samples

elemental analysis (wt.%)					XPS analysis (atom%)		
sample	C	H	N	O	C	N	O
HPNCT	82.15	3.16	2.26	12.43	82.42	1.18	16.4
HPNCT-600	83.96	1.69	1.98	12.37	83.56	0.88	15.56
HPNCT-700	84.99	0.97	1.87	12.17	87.46	1.29	11.25
HPNCT-800	90.38	0.25	1.56	7.81	91.51	1.41	7.08

Table 3. XPS Peak Positions and Relative Surface Concentrations of Nitrogen Specific Obtained by Fitting the N 1s Spectra

Sample	Pyridinic-N	Pyrrolic/pyridone-N	Quaternary-N	Pyridine-N-oxide
HPNCT	31.39	32.91	22.82	12.88
HPNCT-600	21.6	42.6	23.7	12.1
HPNCT-700	29	34.3	25.5	11.2
HPNCT-800	26.22	33.7	29.2	10.88

Table 4.Comparison of energy density and power density of various carbon materials with willow catkins derived carbon

Waste biomasses	Elemental analysis (wt.%)			Ash (%)	Ref.
	C	H	N	Ash	
Palm stem	45.56	5.91	0.82	4.02	S7
Bamboo	45.53	4.61	0.22	6.51	S8
Durian shell	39.30	5.90	1.00	4.84	S9
Banana empty fruit bunch	41.75	5.10	1.23	15.73	S10
Pomegranate seed	49.65	7.54	4.03	1.83	S11
Wheat straw	46.50	6.30	0.90	3.23	S12
Bagasse	41.55	5.55	0.03	6.2	S13
Rice husk	36.52	4.82	0.86	16.7	S13
Willow catkin	47.11	5.89	0.83	1.12	Our work

A graphical abstract

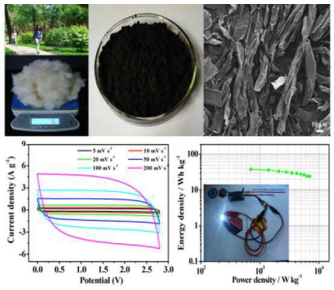

Hierarchical porous carbon microtubes derived from willow catkin exhibited excellent electrochemical performances in both the aqueous and organic electrolyte.